

# Wave-mode separation in the complex wavelet domain using combined translational and rotational data

*Ohad Barak and Shuki Ronen*

## ABSTRACT

Rotations are medium strains induced by seismic waves, which are independent of the commonly-recorded translational motions. We use combined translational data from geophones and rotational data from rotation sensors to identify and separate particular wave modes from a six-component (6C) field dataset. We develop a polarization filter in the complex wavelet domain in order to identify and subsequently attenuate shear and surface wave modes. Our method does not rely on spatial continuity parameters, and can therefore be applied to spatially aliased data.

## INTRODUCTION

Rigid bodies in a three dimensional world have six degrees of freedom: three components of translation and three components of rotation. The time derivatives of translations are the particle velocities and the rotations are the pitch, roll and yaw, as shown in the following table:

Axis	Translation		Rotation	
Z	Vertical	$v_z$	Yaw	$r_z$
X	Radial	$v_x$	Roll	$r_x$
Y	Transverse	$v_y$	Pitch	$r_y$

where  $v_i$  are particle velocities along the  $i$  axis, and  $r_i$  are rotation rates around the  $i$  axis.

A hydrophone records the divergence of the particle displacement wavefield

$$P = \kappa (\nabla \cdot \vec{u}), \quad (1)$$

where  $\vec{u}$  are particle displacements and  $\kappa$  is the bulk modulus of the water to which hydrophones are coupled. Rotations are a measurement of the curl of the particle displacement wavefield

$$\vec{R} = \frac{1}{2}(\nabla \times \vec{v}), \quad (2)$$

and are a recording of the anti-symmetric strains of the medium (Cochard et al., 2006).

The rotational components can be used to enhance vertical geophone data (Muyzert et al., 2012), and spatial aliasing of high-wavenumber arrivals can thus be mitigated. Edme et al. (2014) treat rotational data as a noise model for ground-roll, and use adaptive subtraction in order to remove ground roll from the vertical component of geophone land data. In Barak et al. (2014) we've shown that rotation data are extra information, are independent of geophone data, and can be used in conjunction with geophone data to identify and separate wave modes on all recorded components using singular-value decomposition polarization analysis.

In this paper, we further develop our multicomponent polarization analysis method by first transforming the data to the complex wavelet domain. The Complex Wavelet Transform (CWT) enables us to use frequency as an additional instantaneous attribute by which to identify and separate wave modes.

We apply our method to a 2D dataset acquired by Chevron near the Kettleman hills in California, which included collocated 3C geophones and 3C electrokinetic rotation sensors.

## Estimating rotational motion from geophone data

The stress-displacement relation for tangential stresses reads:

$$\sigma_{ij} = \mu (\partial_j u_i + \partial_i u_j), \quad (3)$$

where  $\sigma_{ij}$  are the tangential stresses,  $u_i$  are particle displacements and  $\mu$  is the shear modulus.

At a free surface, or at an interface between a medium with shear strength and one without shear strength (such as the ocean-bottom interface), the tangential stresses  $\sigma_{ij}$  are zero. Therefore, assuming we have receivers laid out on a flat free surface, we have

$$\begin{aligned} \partial_z u_y &= -\partial_y u_z, \\ \partial_z u_x &= -\partial_x u_z, \end{aligned} \quad (4)$$

meaning that the vertical derivative of the horizontal displacement component is equal to the horizontal derivative of the vertical displacement component.

Rotation is defined as the curl of the wavefield. Since our geophones record the time derivative of displacement (particle velocity), we use the time derivative of rotation, or rotation rate:

$$\begin{aligned}
\vec{r} = \frac{1}{2}(\nabla \times \vec{v}) &= \hat{X} (\partial_y v_z - \partial_z v_y) / 2 \\
&+ \hat{Y} (\partial_z v_x - \partial_x v_z) / 2 \\
&+ \hat{Z} (\partial_x v_y - \partial_y v_x) / 2,
\end{aligned} \tag{5}$$

where  $\hat{X}$ ,  $\hat{Y}$  and  $\hat{Z}$  are the rotation axes. Substituting equation 4 into 5, we see that at a free surface interface

$$r_x = \partial_y v_z, \quad r_y = -\partial_x v_z, \quad r_z = \frac{1}{2} (\partial_x v_y - \partial_y v_x), \tag{6}$$

i.e., the horizontal rotation-rate components can be derived from closely-spaced vertical geophones, and the vertical rotation-rate component can be derived from closely-spaced horizontal geophones. The distance between geophones that will ensure reliability of the differencing depends on the horizontal wavenumbers that present in the data. The sensors must be close enough to each other to prevent aliasing, but not so close that the decrease in signal to noise ratio associated with the differencing significantly degrades the signal.

## Complex wavelet transform

The complex wavelet transform is defined as:

$$C_i(a, b; g_i(t), \psi(t)) = \int_{-\infty}^{\infty} g_i(t) \frac{1}{\sqrt{a}} \psi^* \left( \frac{t-b}{a} \right) dt, \tag{7}$$

where  $g_i(t)$  is the input signal of the  $i^{th}$  data component,  $\psi(t)$  is a mother wavelet,  $\psi^*$  is a daughter wavelet, which is the complex conjugate of the mother wavelet stretched by scale  $a$  and time-shifted by  $b$ . It is common to use the Morlet wavelet as a mother wavelet, and we do so in this paper. For brevity, we will use  $C_i(a, b) := C_i(a, b; g_i(t), \psi(t))$

The complex wavelet transform effectively shows how correlated our time-series is with a particular daughter wavelet. Since the correlation is done in running time windows (shifted by  $b$ ), the transform retains the temporal sense of the data and yet decomposes it to wavelet scales, which are in essence similar to frequency. We use this time-frequency decomposition to identify wave modes of particular frequencies that appear at particular times in the data.

## Singular value decomposition in the complex wavelet domain

de Meersman et al. (2006) apply singular value decomposition (SVD) on the analytic signal of three-component geophone data in order to estimate the polarization of

P-wave arrivals and extract them from noisy data. The use of the analytic signal enables a determination of the ellipticity of a particular arrival, which is an attribute associated with Rayleigh waves.

SVD, however, is a mathematical tool that can be applied to any data series, and it is similarly possible to apply SVD on 6-component data comprising 3C geophone and 3C rotation sensor data. The resulting polarization vectors indicate not only linear polarization, but also rotational polarization, though there is no intuitive understanding of the particle motion these polarization vectors represent.

We posit that rotational motion is a better indicator of wave modes than are elliptical particle motions, since rotations are medium strains (eq. 2), whereas particle displacements are not. Particularly, when considering the different nature of the strains induced by P-waves versus shear or surface waves, we would expect to see significant differences in the relative amounts of rotation generated by each wave mode.

Wave modes may also be differentiated by their frequency bands. One mechanism that can account for this effect is attenuation, which affects shear waves and surface waves more than it does P-waves as a result of the shorter wavelengths that shear and surface waves have. Using the complex wavelet transform of the multicomponent translational and rotational data, we combine multiple attributes by which wave modes may be separated.

We apply SVD to a time slice of a single complex-wavelet transformed 6C trace  $C_i(a, b_k)$ , where  $b_k$  is the time index of the slice,  $a$  are the wavelet scales and  $i$  represents the data component. Therefore, we have an  $N_a \times 6$  data matrix where the rows are the wavelet scales and the columns are the components  $\mathbf{D} = [v_z(a), v_x(a), v_y(a), r_z(a), r_x(a), r_y(a)]$ . SVD is a method of finding the waveform  $\mathbf{u}$ , magnitude  $\sigma$ , and polarization  $\mathbf{v}$  of the signal that is present in the data  $\mathbf{D}$ . The SVD of the data  $\mathbf{D}$  is given by

$$\mathbf{D} = \mathbf{U}\Sigma\mathbf{V}^T, \quad (8)$$

where  $\mathbf{D}$  is the product of the  $N_a \times 6$  matrix  $\mathbf{U}$ , the 6x6 diagonal matrix  $\Sigma$ , and the transpose of the 6x6 matrix  $\mathbf{V}$ . The unit left and right singular vectors  $\mathbf{u}_i$  and  $\mathbf{v}_i$  are the six column-vectors of  $\mathbf{U}$  and  $\mathbf{V}$ . The singular values  $\sigma_i$  are the diagonal elements of  $\Sigma$ . They are ordered such that  $|\sigma_1|$  is the greatest and  $|\sigma_6|$  the smallest. The left and right singular vectors are mutually orthogonal, such that  $\mathbf{U}^T\mathbf{U} = \mathbf{I}$  and  $\mathbf{V}\mathbf{V}^T = \mathbf{I}$ .

The right singular vectors  $\mathbf{v}_i$  display the polarization of the data within the particular frequency window along the six axes. We transpose and multiply the matrix  $\mathbf{V}$  by the singular value matrix  $\Sigma$ , to obtain the scaled polarization vectors:

$$\mathbf{s} = \sigma\mathbf{v}^T. \quad (9)$$

Applying CWT to a time window of a particular multicomponent trace in the data where an undesired wave mode dominates, and then applying SVD to the transformed data, we arrive at the frequency-dependent template polarization of the undesired wave mode  $\mathbf{s}_{\text{temp}}(a)$ .

We scan the data searching for polarizations similar to the particular wave mode's polarization template on a trace by trace basis. The similarity measure is configurable, and can be tuned to be more restrictive or more permissive. Where we find energy with complex polarization similar to the template, we attenuate the first polarization vectors  $s_1(a)$ . Attenuation is done by applying a weighting function only to the first singular value of  $\Sigma$ . The weighting is both a function of the similarity of the current frequency window's polarization to the template polarization, and also of the wavelet scale  $a$ , where greater damping is applied to higher scales (lower frequencies).

After weighting the first singular value, the data are reconstructed:

$$\mathbf{D} = \mathbf{U}\mathbf{W}\Sigma\mathbf{V}^T. \quad (10)$$

An inverse CWT is then applied to the reconstructed data. Since we do not rely on any additional spatial considerations, the method is effectively insensitive to spatial aliasing in the data.

## THE KETTLEMAN SIX-COMPONENT SURVEY

The 2D Kettleman survey comprised four types of sources and multiple types of receivers, both on the surface and at depth. The shot line length was 1.6 km long. At one end of the shot line there were five 3C linear accelerometers, which were closely spaced at a 2.1 m interval inline. In between the accelerometers in the inline direction there were four 3C electrokinetic rotation sensors. The rotational components were aligned to coincide with the direction of the linear components, so that the positive sense of rotations around the vertical, radial and transverse axes was according to the right-hand rule.

The following figures show the 6C receiver gather for the four source types at one receiver station. Figures 1(a)-1(f) are accelerated weight-drop data, Figures 2(a)-2(f) are vibroseis data, Figures 3(a)-3(f) are 25 m depth dynamite data, and Figures 4(a)-4(f) are 50 m depth dynamite data. All data are clipped at 93%.

The strong ground roll in the accelerated weight-drop data is not aliased due to a very small shot interval of 6.25 m. All other sources were shot with a 25 m shot interval, and therefore exhibit significant aliasing of the ground roll. The best reflection signal appears on the dynamite data, as it excites less ground roll than surface sources.

However, note how the rotation-sensor data for the dynamite sources in Figures 3(d)-3(f) and Figures 4(d)-4(f) have a very low signal to noise ratio. This would make

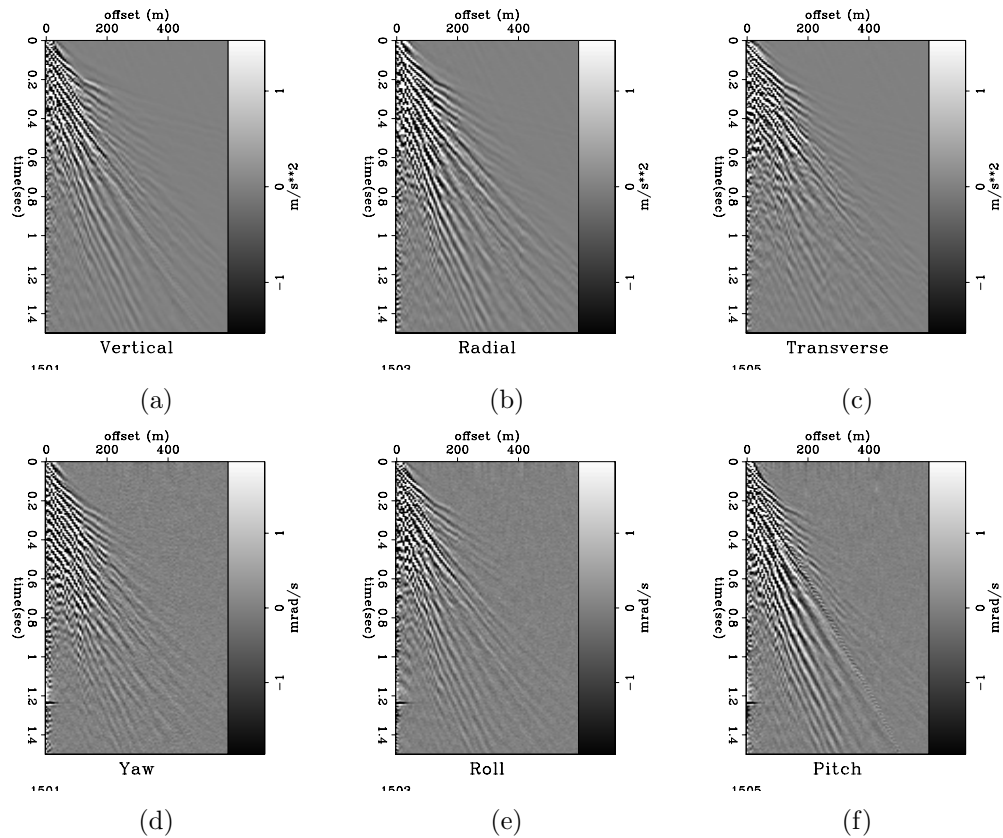


Figure 1: 6C receiver gather of the accelerated weight-drop source, clipped at 93%. Shot spacing was 6.25 m. Six shots were executed at each station, and then diversity stacking was applied to increase the signal to noise ratio. The data observable in these sections at this clip level consist entirely of various Rayleigh wave modes, which are not aliased due to the very close shot spacing. [ER]

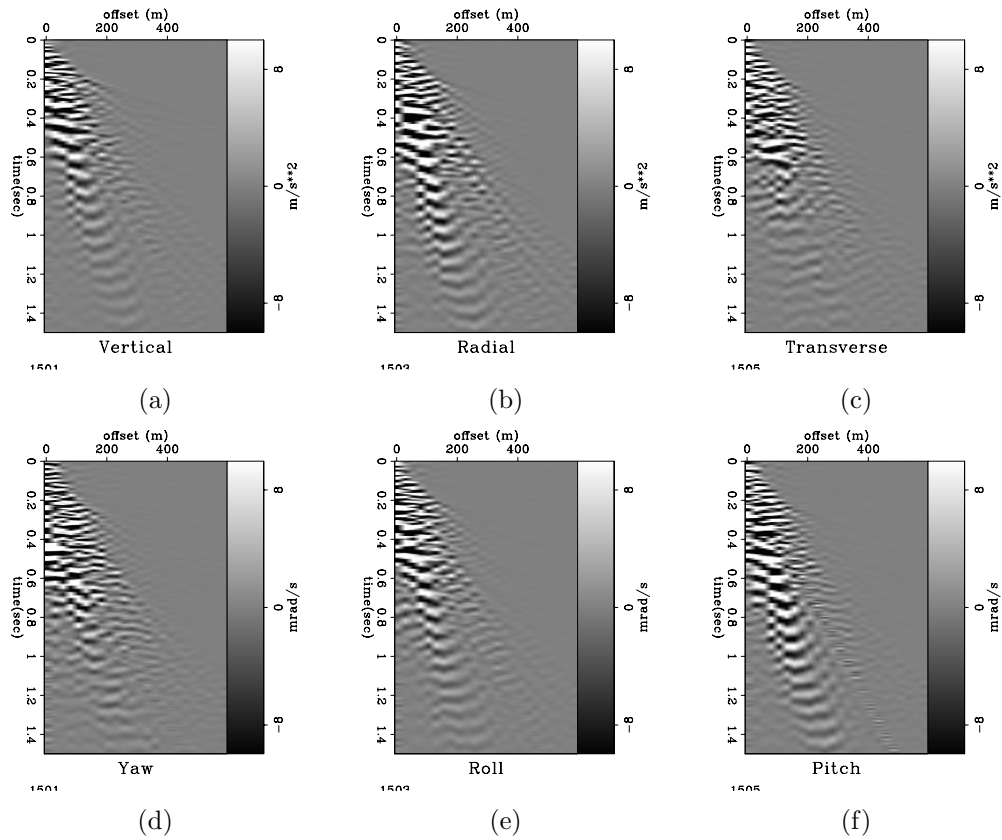


Figure 2: 6C receiver gather of the vibroseis source, clipped at 93%. Shot spacing was 25 m, and so the various Rayleigh wave modes are aliased. Some P-wave reflections are visible at early times. [ER]

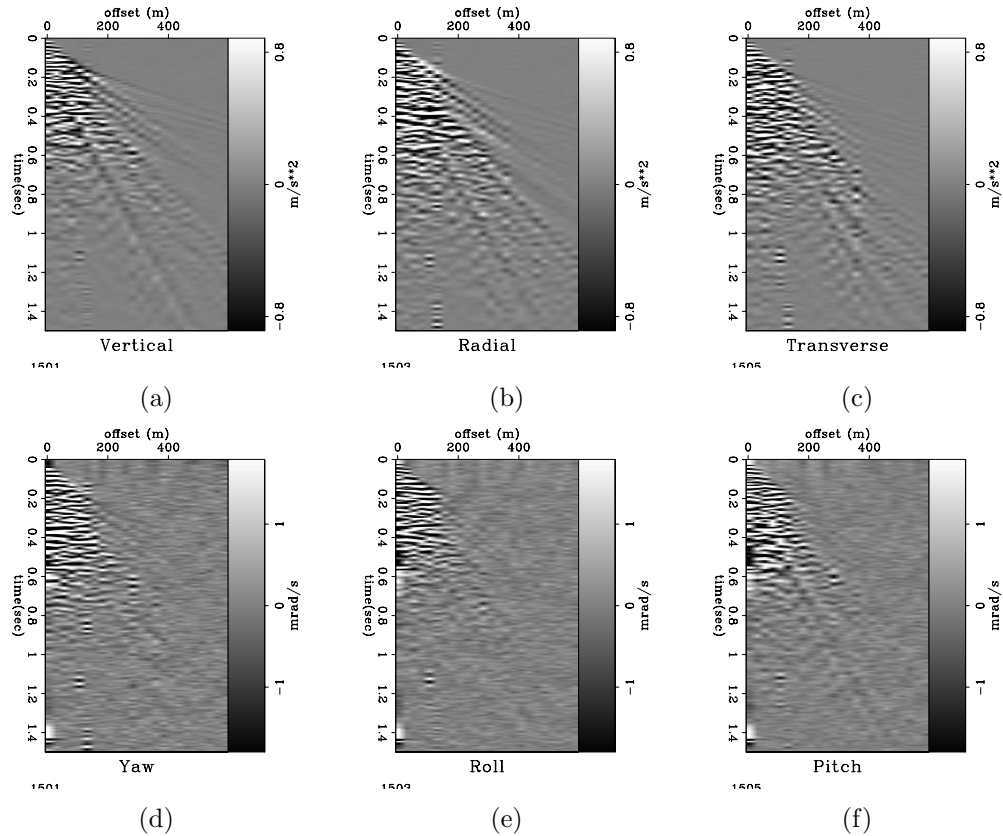


Figure 3: 6C receiver gather of the 25 m depth dynamite source, clipped at 93%. Shot spacing was 25 m. Compared to the accelerated weight drop and vibroseis surface sources, the amount of ground roll in these data is much lower, though aliasing is still very significant. Some reflections are visible at early times from offset 200 m and on. Note how the signal to noise ratio of the rotation-sensor data is low in (d), (e) and (f). [ER]

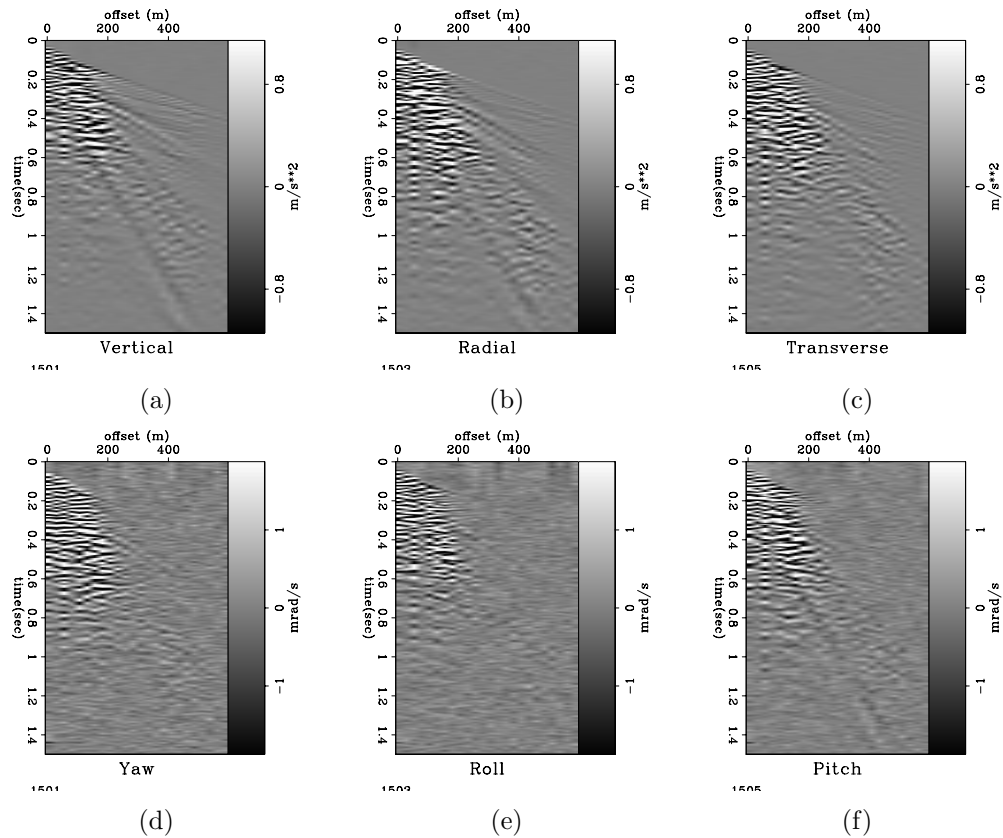


Figure 4: 6C receiver gather of the 50 m depth dynamite source, clipped at 93%. Shot spacing was 25 m. Reflection data are more visible in these sections vs the 25 m depth dynamite source. We note a particular low-frequency arrival starting from  $t = 0.35$  s at offset=200 m, which appears to be shear-induced energy. Again, note the low signal to noise ratio for the rotational data in (d), (e) and (f). [ER]

any multicomponent analysis involving rotational data difficult. We therefore opted to use vertical geophone-differencing (eq. 6) in order to extract a better-quality pitch rotational signal.

Figures 5(a) and 5(c) are the pitch component acquired by the rotation sensor for the vibroseis and dynamite sources, respectively. Figures 5(b) and 5(d) are the pitch component calculated by differencing the two vertical accelerometers adjacent to the rotation sensor (in the inline direction). Note how the pitch component derived from the differencing has a better signal to noise ratio than the rotation-sensor at larger offsets.

Unfortunately, there were no accelerometers placed in the crossline direction, therefore we were not able to similarly calculate the roll or the yaw rotational components by geophone differencing as in equation 6.

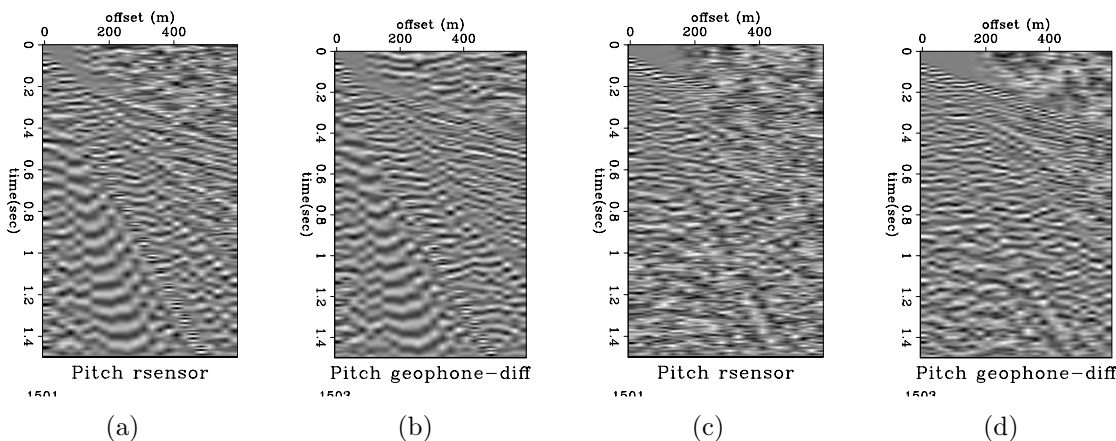


Figure 5: Comparison of pitch component acquired by rotation sensor and pitch calculated by differencing adjacent geophones. (a) Rotation sensor pitch for vibroseis source. (b) Geophone-differencing pitch for vibroseis source. (c) Rotation sensor pitch for 50 m depth dynamite source. (d) Geophone-differencing pitch for 50 m depth dynamite source. Note that for both source types, the signal to noise ratio of the pitch derived from geophone differencing is much higher at larger offsets than the pitch measured by the rotation sensor. AGC with a window size of  $t = 0.2$  s has been applied to the data for display. [ER]

## POLARIZATION IN THE COMPLEX WAVELET DOMAIN

Our purpose is to separate wave modes in the data using all components. There are desirable wave modes which we term “data”, and undesirable ones which we call “noise”. Most commonly in seismic data, the wave modes of interest are the P-wave reflections, as these provide information about the subsurface at depth. Surface waves and shear induced energy appearing on the vertical component are considered to be noise, as they obscure the P-wave reflections.

Figures 6(a)-6(d) are the vertical component receiver gathers for the four source types, after application of NMO to flatten the P-wave reflections. In this display, events that are not close to being flat are necessarily noise.

Note the strong ground roll in Figures 6(a) and 6(b), which prevents us from observing the near-offset reflections (a common issue in seismic land data). However, it would not be possible to use filters that rely on spatial sampling to remove the ground roll from the vibroseis data because they are aliased. A low-pass filter would first need to be applied to remove all the aliased energy. However, that would result in significant elimination of reflection data as well.

The 50 m depth dynamite source data in Figure 6(d) has the best reflection signal. However, observe the non-flat lower frequency arrival starting at  $t = 0.3$  s and at offset=200 m. This event is the result of shear-induced energy, possibly a scattering off an anomaly in the near surface. It is visible on all components in Figures 4(a)-4(f) and, like the ground roll for the surface sources, it obscures the P-wave reflections. We therefore target this arrival for removal from the 50 m depth dynamite data.

We do not, however, have reliable rotation data for the yaw and roll components. Therefore, for the analysis that follows we used only three components out of the available six: the vertical, radial and pitch. Since the survey was 2D, most of the seismic energy appears on these components.

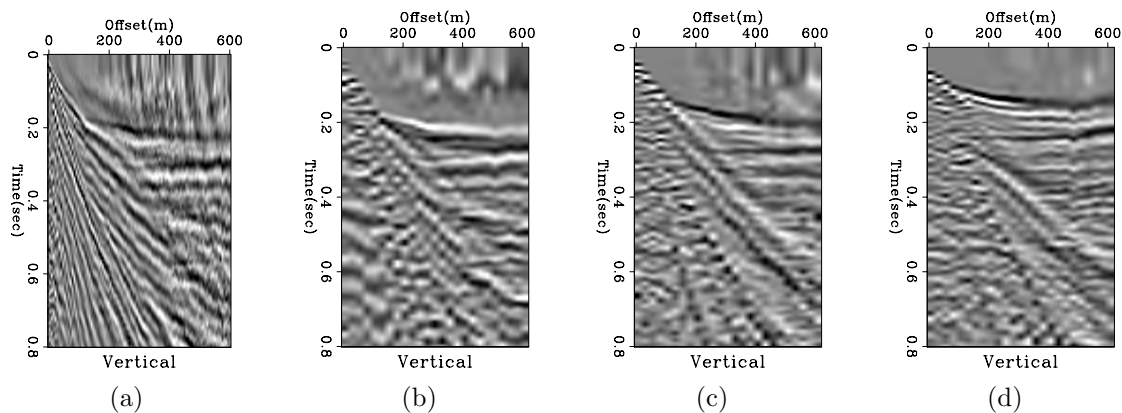


Figure 6: Receiver gathers of the vertical geophone component of the 4 source types in the Kettleman survey, after NMO with velocity  $v = 1700$  m/s. (a) Accelerated weight drop. (b) Vibroseis source. (c) Dynamite charge at 25 m depth. (d) Dynamite charge at 50 m depth. Source (a) was acquired with 6.25 m shot spacing, while (b), (c) and (d) were done with 25 m shot spacing. Observe the generally higher quality reflections acquired with the dynamite sources. The two surface sources (a) and (b) generate much more ground roll. AGC with a window size of  $t = 0.2$  s has been applied to the data for display. [ER]

## Filtering of a particular wave mode from the 50 m depth dynamite data

Figure 7(a) is the three-component trace comprising the vertical, radial and pitch components from the 50 m depth dynamite source at offset 280 m. The pitch component was derived by vertical-geophone differencing as a result of the low SNR on the pitch rotation sensor data.

Figures 7(b), 7(c) and 7(d) are the CWT of the respective three components of the trace. For wavelet scale 0 the corresponding frequency is 125 Hz, and at wavelet scale 8 the corresponding frequency is 0.5 Hz. Observe that between  $t = 0.2$  s and  $t = 0.3$  s there are P-wave reflections, and that these reflections correspond to lower wavelet scales (higher frequencies) in the complex wavelet domain of all the components. At  $t = 0.4$  s there is a shear-induced arrival, which appears in the wavelet domain as a higher scale feature (lower frequency). However, this feature is more significant on the vertical and radial components than on the pitch component.

These two distinguishing attributes of the shear arrival: lower frequency and different appearance in the wavelet domain of the various data components, are what we use to identify and attenuate it.

Figure 8(a) shows the time slice of the CWT of the three data components of the same trace, at time  $t = 0.22$  s where there are P-wave reflections. We apply SVD to this slice as described in equation 8, and display the scaled polarization vectors as in equation 9 in Figures 8(b), 8(c) and 8(d). Each row in these figures represents one polarization vector. Note the pattern visible for the first polarization vectors, which indicates that the energy at this time has both high frequency and lower frequency polarization.

Figure 9(a) shows the time slice of the CWT of the three data components at time  $t = 0.42$  s, which is the shear-arrival time. The scaled polarization vectors are shown in Figures 8(c), 8(c) and 8(c). For this arrival, the first polarization vectors show a very different pattern compared to Figure 8(b), and indicate that for this time the polarization is largely on the lower frequencies and on the vertical and radial components.

The 2nd polarization vectors, however, have higher frequencies, more like the 1st polarization vectors of the P-wave reflections. This indicates what we can already see from the data in Figure 6(d): the shear arrival is obscuring the P reflections.

Our template polarization  $\mathbf{s}_{\text{temp}}$  is then Figure 8(c), and it is this polarization which we search for in the data on a trace by trace basis.

Figure 7(e) shows the weights which are applied to the complex first polarization vectors of the multicomponent trace. Note how the higher scales (lower frequencies) are preferentially damped. However, note that this is not simply a weighting down of low frequencies. The weighting function depends on the similarity of the first polarization vectors at each time and at each frequency to the template polarization

in Figure 8(c). Where there is a similarity, the lower frequencies are preferentially weighted down.

Figures 10(a), 10(b) and 10(c) are the vertical, radial and pitch components before application of the complex polarization filtering, while Figures 10(d), 10(e) and 10(f) are the same components after application of the polarization filtering. Note that the shear-induced arrival that we targeted for removal has indeed been attenuated, and the P-wave reflection signal which was hidden below it has been enhanced. The P-wave reflections appear continuous.

Note also that we used only one time window of one trace to determine the polarization template of this shear energy, and yet after applying the filtering based on that polarization template to the entire dataset the shear energy has been attenuated everywhere and for all components.

Figure 11(a) is again the vertical component after the polarization filtering, while Figure 11(c) shows the frequency spectra of these data. Compare this to a low-cut filter, where the pass band was 25 Hz - 60 Hz, shown in Figure 11(b). There is an improvement in continuity of the P-wave reflections, but the shear energy is still apparent. The resolution of the P reflections, however, has been degraded because of the simple frequency filter. Comparing Figures 11(c) and 11(d), we see that unlike standard frequency filtering, the polarization filtering has not performed a wholesale removal of the low frequencies.

## Filtering of aliased ground roll from the vibroseis data

The vibroseis data contain strong ground roll, which are much stronger than the P reflections at near offsets. Figures 12(a), 12(b) and 12(c) are the vertical, radial and pitch components before application of the complex polarization filtering. A very slow Rayleigh wave mode is visible beginning from  $t = 0.2$  s and ending at  $t = 0.8$  s at offset 200 m.

To estimate the polarization template, we windowed out four traces containing this slow Rayleigh wave mode around  $t = 0.6$  s. We then applied the same polarization filtering method as we did for the dynamite data.

Figures 12(d), 12(e) and 12(f) are the vertical, radial and pitch components after application of the polarization filtering. Though the improvement in the data is not drastic, we do observe that there are two horizontal events that appear from under the ground roll on the vertical component, at times  $t = 0.4$  s and  $t = 0.58$  s. As before, the attenuation of the wave mode that we targeted has occurred on all components.

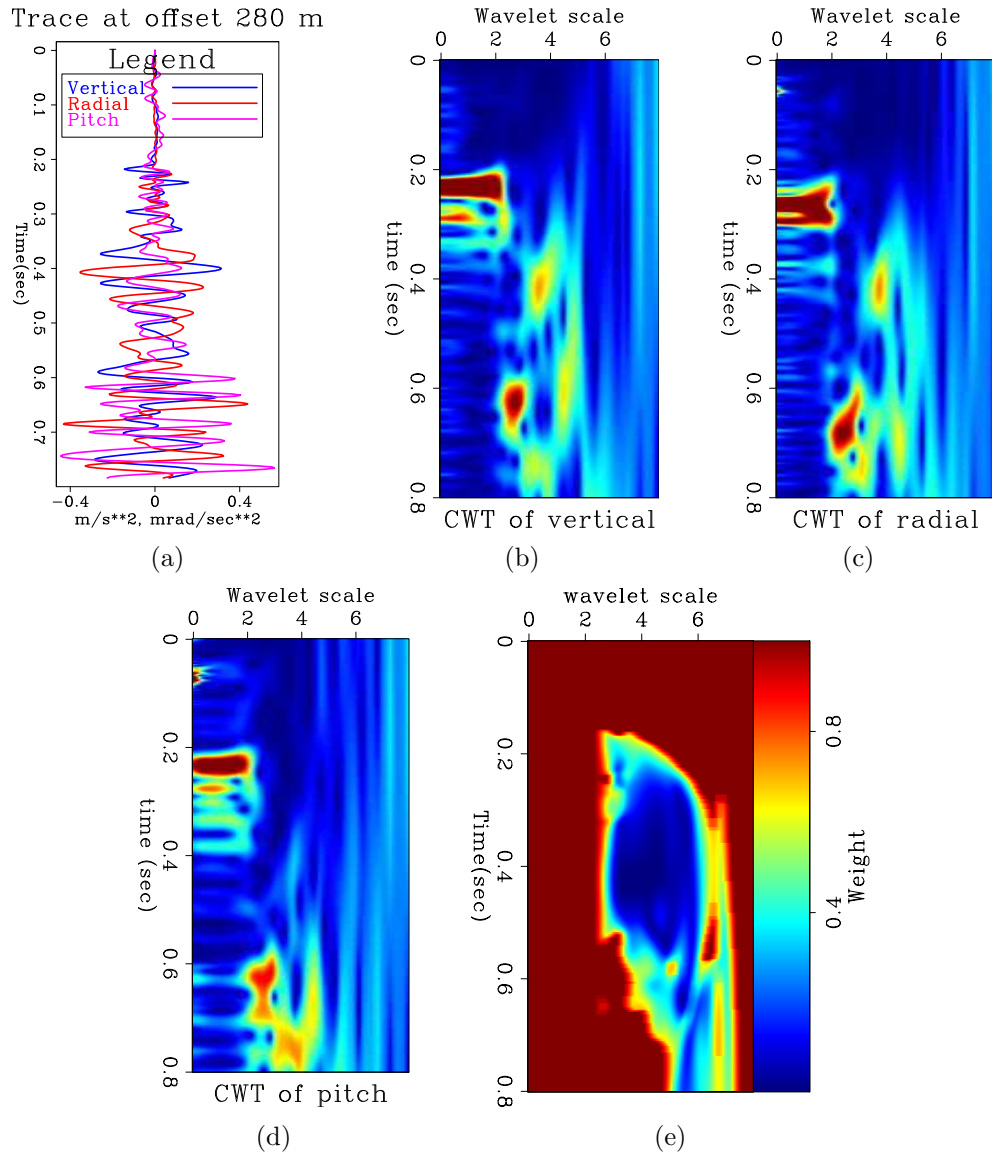


Figure 7: (a) Trace of the vertical geophone, radial geophone and pitch component derived from geophone differencing, from the 50 m depth dynamite source at offset 280 m. The absolute values of the complex wavelet transform are shown for (b) vertical component, (c) radial component, and (d) pitch component. The wavelet scale is dyadic, beginning from a frequency of 125 Hz at wavelet scale 0 down 0.5 Hz at wavelet scale 8. Up until  $t = 0.32$  s, the data contain P reflections, while between  $t = 0.32$  s and  $t = 0.52$  s there is a shear-wave arrival. The lower frequency of the shear arrival can be discerned at  $t = 0.4$  s, for wavelet scale=3.5. (e) The weighting function applied to the components in the wavelet domain to damp the shear wave mode appearing at  $t = 0.4$  s. [ER]

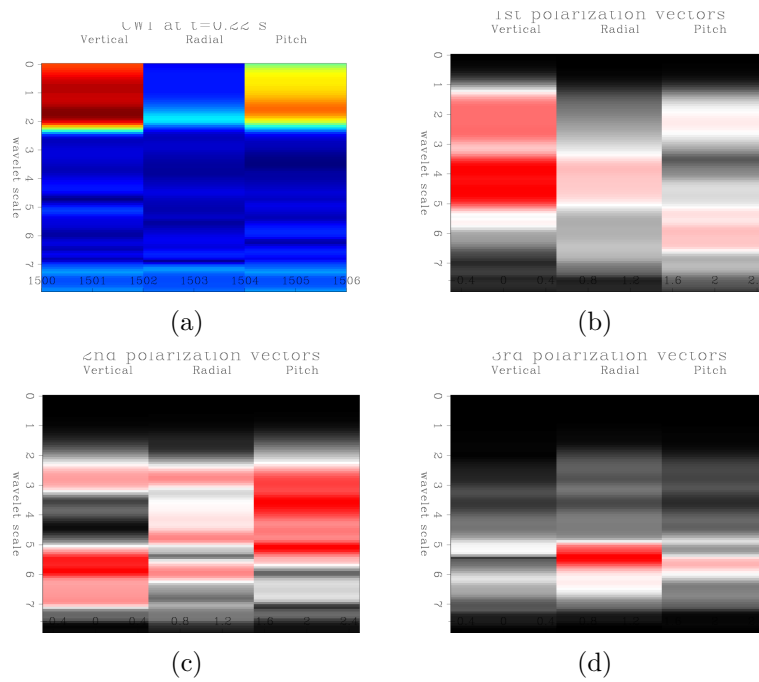


Figure 8: A 3C time slice of the complex wavelet transform of the trace at offset 280 m at  $t = 0.22$  s where a P-wave reflection is visible, and the corresponding absolute values of the complex polarization vector-set for this time slice. (a) Complex wavelet time slice. (b) 1st polarization vectors. (c) 2nd polarization vectors. (d) 3rd polarization vectors. **[ER]**

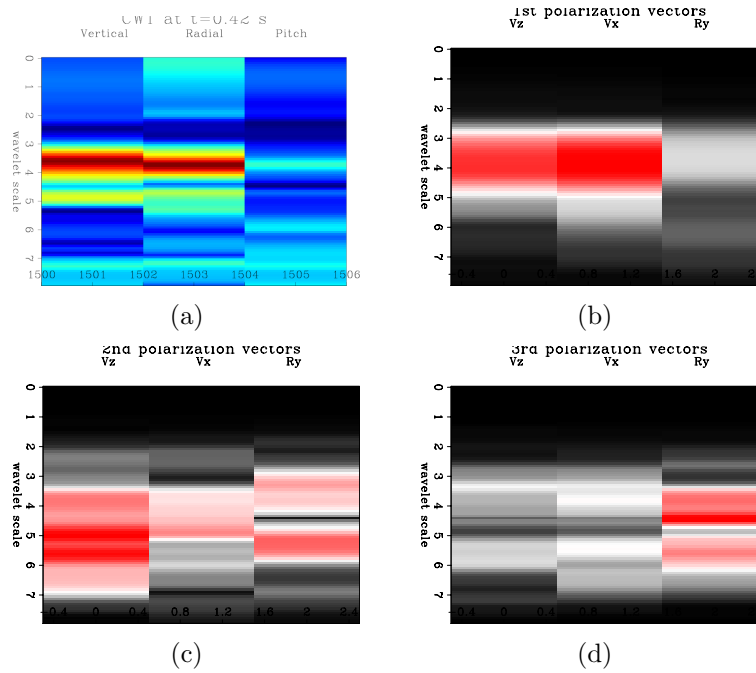


Figure 9: A 3C time slice of the complex wavelet transform of the trace at offset 280 m at  $t = 0.42$  s where shear-wave energy dominates, and the corresponding absolute values of the complex polarization vector-set for this time slice. (a) Complex wavelet time slice. (b) 1st polarization vectors. (c) 2nd polarization vectors. (d) 3rd polarization vectors. Note that the 2nd polarization vectors at (c) have some higher frequency components (lower scales), similar to the 1st polarization vectors at 8(b), indicating that the dominant shear-wave energy in (b) is overlaying weaker P-wave reflection energy. [ER]

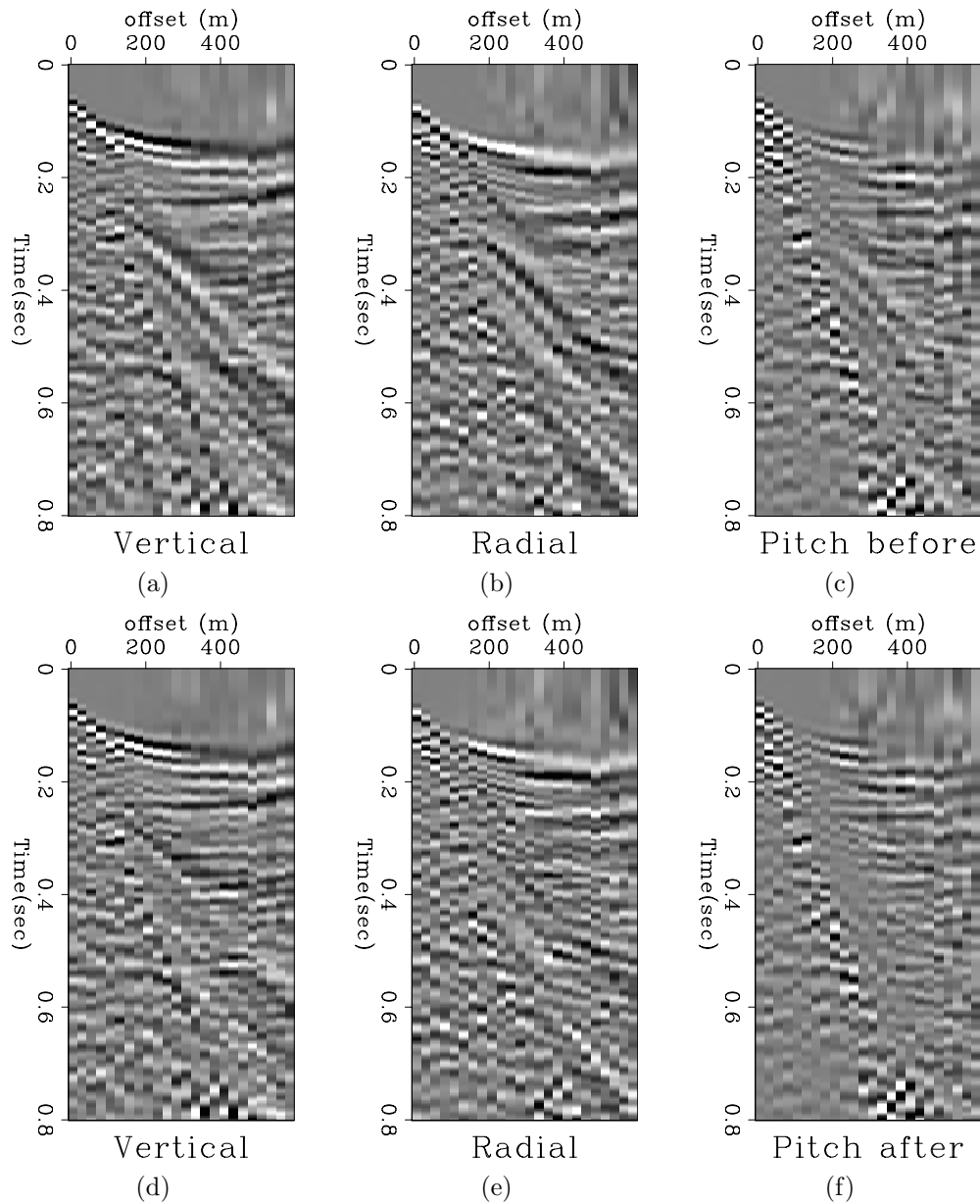


Figure 10: Data components before (top row) and after (bottom row) polarization filter to damp shear energy. (a) Vertical component. (b) Radial component. (c) Pitch component. (d) Vertical component. (e) Radial component. (f) Pitch component. Data are shown after NMO with velocity  $v = 1700$  m/s to flatten the P-wave reflections. AGC with a window size of  $t = 0.2$  s has been applied for display purposes. Observe that the shear induced energy has been attenuated, and that the underlying P-wave reflections are visible after filtering. [ER]

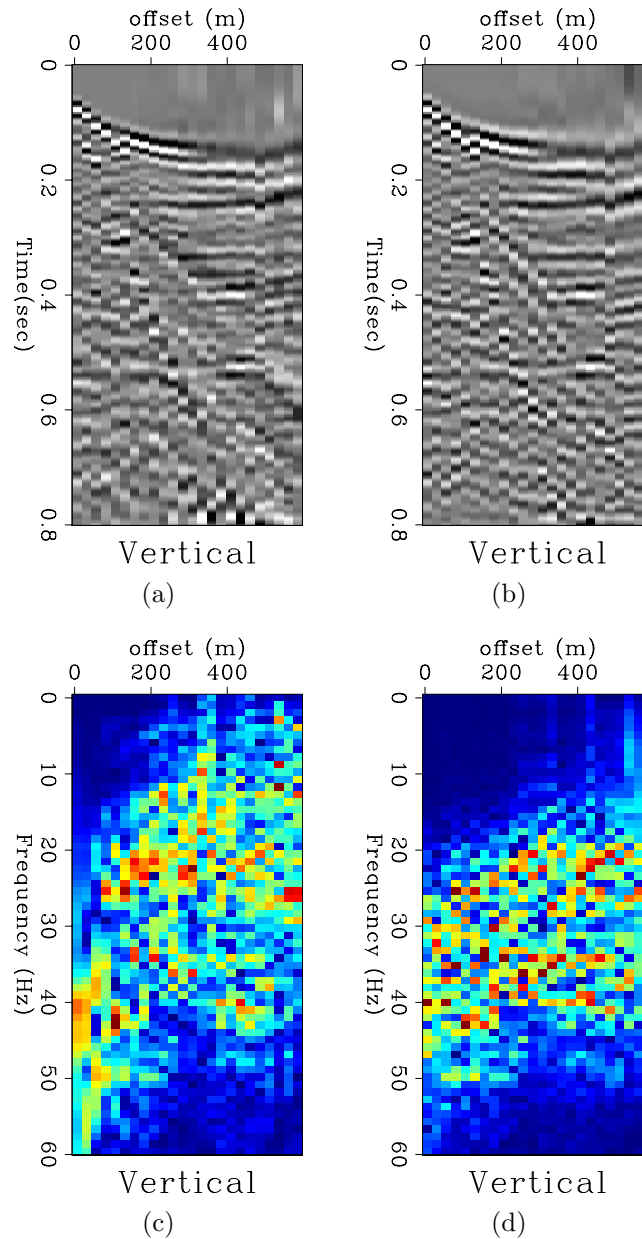


Figure 11: A comparison of the filtering results using complex wavelet polarization filter versus a standard low-cut filter on the 50 m depth dynamite receiver gather. (a) Vertical component after application of complex wavelet polarization filter. (b) Vertical component after application low cut filter, where the pass band was 25 Hz - 60 Hz. (c) Vertical component (a) in the frequency domain. (d) Vertical component (b) in the frequency domain. Observe how in (a) and (c), the polarization filtering does not impartially remove low frequencies, unlike the low cut filter in (b) and (d), and therefore there is no reduction in the resolution of the reflections. [ER]

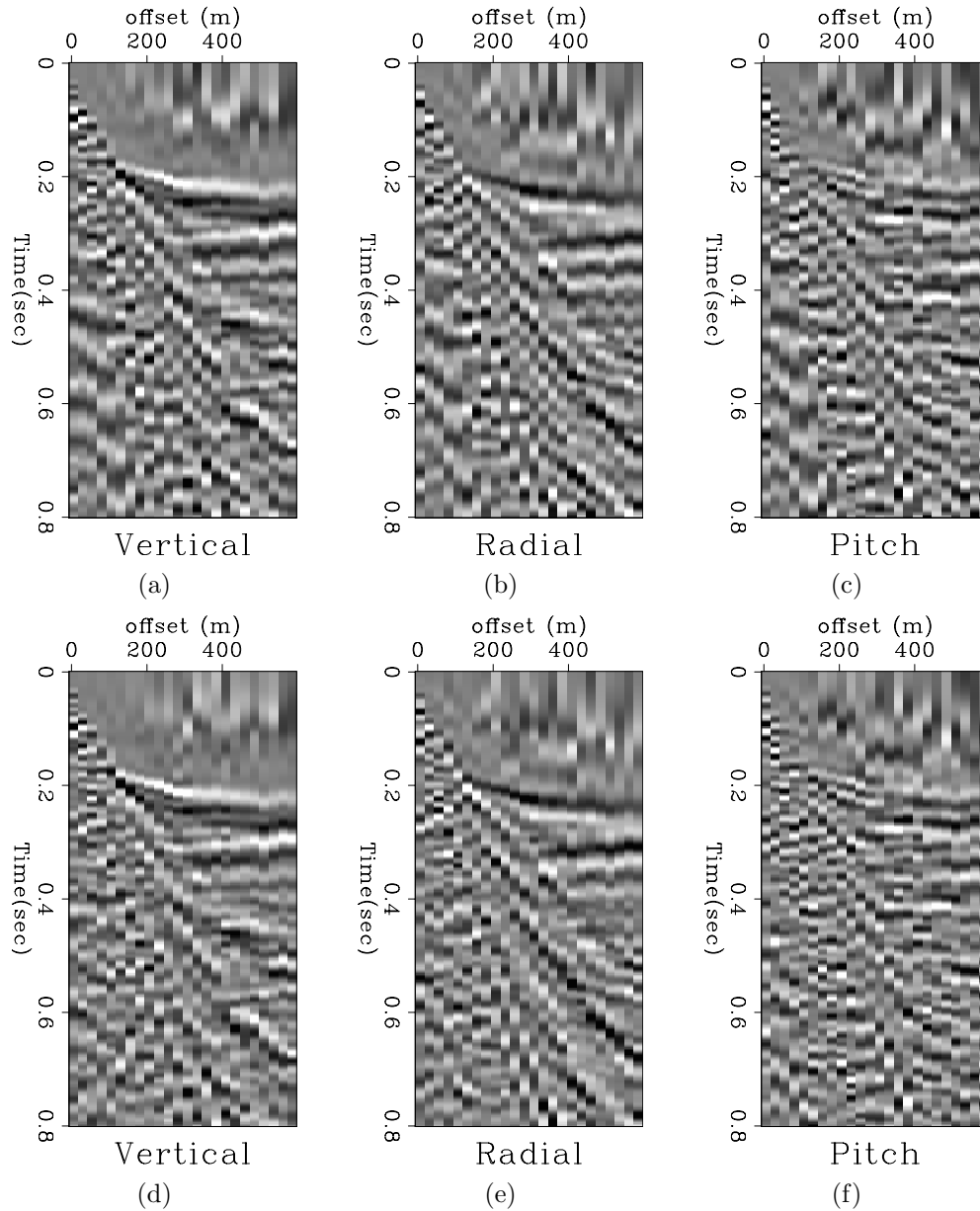


Figure 12: Data components before (top row) and after (bottom row) polarization filter to damp ground-roll energy. (a) Vertical component. (b) Radial component. (c) Pitch component. (d) Vertical component. (e) Radial component. (f) Pitch component. Data are shown after NMO with velocity  $v = 1620$  m/s to flatten the P-wave reflections. AGC with a window size of  $t = 0.2$  s has been applied for display purposes. Observe that the slow ground-roll energy has been attenuated, and some of the underlying P-wave reflections are visible after filtering at near offsets at  $t = 0.4$  s and  $t = 0.58$  s. [ER]

## DISCUSSION

Throughout this paper we have referred to our method of wave-mode separation as a kind of data domain filtering. However, note that we are targeting particular wave modes, and are able to reliably attenuate only those wave modes. This would not work if we were not also able to identify them.

The complex wavelet domain enables us to identify wave modes based on their multicomponent polarization vectors at each frequency, while retaining the temporal sense of the data. Therefore, the filtering is done in a very targeted manner, exactly where it is needed in time and space. The rotational components provide additional control by providing another orthogonal data axis along which to identify wave-mode polarizations. We have shown that the method is successful in attenuating a particular wave mode (shear, Rayleigh) which obscures other weaker wave modes of interest (P-wave reflections). Like all polarization filtering methods, our method has no spatial sampling requirements, and will work on spatially aliased data.

However, the connection between wave modes and polarization of data components is not obvious, and we have no analytic model for determining how each wave mode should appear on any given component at any particular offset. One method of tackling this issue is to use data science methods, a small sample of which we show here: the polarization template is learned from the data. A more comprehensive method would be to classify the polarizations of all wave modes present in massive amounts of 3D seismic data, using a machine learning approach.

## ACKNOWLEDGEMENTS

We thank Chevron for permission to use the Kettleman dataset, and particularly Ranjan Dash for preparing the data for our use. The rotation sensors were provided by Geokinetics. We also thank Robert Brune for many fruitful discussions.

## REFERENCES

- Barak, O., F. Herkenhoff, R. Dash, P. Jaiswal, J. Giles, S. de Ridder, R. Brune, and S. Ronen, 2014, Six-component seismic land data acquired with geophones and rotation sensors: Wave-mode selectivity by application of multicomponent polarization filtering: *The Leading Edge*, **33**, 1224–1232.
- Cochard, A., H. Igel, B. Schuberth, W. Suryanto, A. Velikoseltsev, U. Schreiber, J. Wasserman, F. Scherbaum, and D. Vollmer, 2006, Rotational motions in seismology: Theory, observations, simulation: *Earthquake Source Asymmetry, Structural Media and Rotation Effects*, 391–411.
- de Meersman, K., M. van der Baan, and J. Kendall, 2006, Signal extraction and automated polarization analysis of multicomponent array data: *Bulletin of the Seismological Society of America*, **96**, 2415–2430.

Edme, P., E. Muyzert, and E. Kragh, 2014, Efficient land seismic acquisition sampling using rotational data: 76th EAGE Conference and Exhibition, Seismic Noise Attenuation Session, **ELI1 08**.

Muyzert, E., A. Kashubin, E. Kragh, and P. Edme, 2012, Land seismic data acquisition using rotation sensors: 74th Conference and Exhibition, EAGE, Extended Abstracts.